Microsc. Microanal. 00, 1–8, 2017
doi:10.1017/S1431927617000186

Microscopy AND Microanalysis

Interfaces in Oxides Formed on NiAlCr Doped with Y, Hf, Ti, and B

Torben Boll,[1,*] Kinga A. Unocic,[2] Bruce A. Pint,[2] and Krystyna Stiller[1,*]

[1]*Department of Physics, Chalmers University of Technology, SE-412 96 Göteborg, Sweden*
[2]*Oak Ridge National Laboratory, Materials Science and Technology Division, Oak Ridge, TN 37831, USA*

Abstract: This study applies atom probe tomography (APT) to analyze the oxide scales formed on model NiAlCr alloys doped with Hf, Y, Ti, and B. Due to its ability to measure small amounts of alloying elements in the oxide matrix and its ability to quantify segregation, the technique offers a possibility for detailed studies of the dopant's fate during high-temperature oxidation. Three model NiAlCr alloys with different additions of Hf, Y, Ti, and B were prepared and oxidized in O_2 at 1,100°C for 100 h. All specimens showed an outer region consisting of different spinel oxides with relatively small grains and the protective Al_2O_3-oxide layer below. APT analyses focused mainly on this protective oxide layer. In all the investigated samples segregation of both Hf and Y to the oxide grain boundaries was observed and quantified. Neither B nor Ti were observed in the alumina grains or at the analyzed interfaces. The processes of formation of oxide scales and segregation of the alloying elements are discussed. The experimental challenges of the oxide analyses by APT are also addressed.

Key words: oxidation, diffusion, grain boundaries, reactive elements, atom probe tomography, high-temperature corrosion

Introduction

Today, the most important life-limiting factor of advanced alloys for many high-temperature applications is their limited oxidation/corrosion resistance and not their mechanical degradation.

Essentially all potential metallic materials are unstable in high-temperature environments and the various oxidation processes are highly exothermic. The only reason it is possible to have materials that can be used at all is that the reaction product, the oxide, may form a protective layer on the component surface (Kofstad, 1966).

Thus, the development of methods for surface protection against corrosion and oxidation of high-temperature materials has become an important area in modern material science. The basic principle is to raise, at the surface of an actual component, the amount of that element that forms a protective oxide scale. The oxidation resistance of such an enriched layer (often existing as a coating) is then dependent of its ability to maintain a continuous surface layer of the oxide, which serves as a diffusion barrier and reduces the rate of reaction between oxygen and the underlying metal. In the case of Ni-base superalloys, developed for various high-temperature applications (e.g., turbine blades for aircrafts), the most successful oxidation protection is obtained by the formation of an Al-enriched intermetallic outer layer. During high-temperature exposure in air this layer creates, a protective Al_2O_3-oxide layer, an alumina scale. Alumina is protective as it is dense, slow-growing, well-bonded to the metal and resistant against cracking and spallation (Young, 2016).

Received July 3, 2016; accepted January 16, 2017
*Corresponding authors. torben.boll@kit.edu; stiller@chalmers.se

Diffusion along alumina grain boundaries (GBs) is recognized to be the rate-controlling transport mechanism that might be altered by the presence of alloying elements, but the exact mechanisms affecting diffusional fluxes still remain not entirely understood. One of the important issues is the fate of the base metal elements, most commonly Ni or Cr, in the oxide as solubility of these elements in alumina is quite low. Another is segregation of reactive elements (RE) Zr, Y, Hf, Ce, etc., from the alloy to the alumina GBs [often observed using analytical transmission electron microscopy (TEM)], that is known to influence growth of this oxide. However, the complex interplay between the oxide microstructure, ionic transport, and oxidation kinetics is still not completely understood to large extent due to the lack of atomic scale information (Pint, 1996; Haynes et al., 2002; Naumenko et al., 2016).

The latest development of laser-assisted atom probe tomography (APT) and new specimen preparation methods using focused ion beam (FIB) milling (Larson et al., 2008) opened the possibility for characterization of the thermally grown oxide scales with high sensitivity and nearly atomic spatial resolution. During the last decade, several successful APT investigations of oxides have been reported (Larson et al., 2008; Lozano-Perez et al., 2009; Marquis et al., 2010; Hono et al., 2011; Chen et al., 2012; Stiller et al., 2012; Dong et al., 2013; Viskari et al., 2013; Chen et al., 2014; Stiller et al., 2016). However, APT analyses of thermally grown oxides are far from being routine and there are still many challenges to overcome.

This article concerns APT investigations of oxidation of three NiAlCr alloys with different additions of RE that are mimicking the most commonly used coatings for protection against oxidation at high temperatures in Ni-based

superalloys (Goward, 1998). The purpose of the work was dual: (1) to demonstrate feasibility of APT studies of grain and phase boundaries of the oxides; (2) to provide detailed information about the chemistry of the investigated interfaces in the studied alloys. Major focus was directed toward analysis of interfaces in the inner part of the oxide scales, i.e., below the outermost region formed during the initial oxidation. This part of the oxide is most important for the protection of the alloy against degradation. The work is a first step in a larger project, aimed at a better understanding of transport processes in alumina, here coupling between the amount of segregating dopants and the oxidation rate is of great interest.

Materials

Three different alloys with different amount of REs were selected. The compositions, as determined by inductively coupled plasma atomic emission spectroscopy, of the alloys are (in at%)

- YHf: $Ni_{62.3}Cr_{15.1}Al_{22.5}Y_{0.03}Hf_{0.04}C_{0.024}$
- YHfTi: $Ni_{61.9}Cr_{15.2}Al_{22.6}Y_{0.020}Hf_{0.043}Ti_{0.31}C_{0.017}$
- YHfB: $Ni_{60.6}Cr_{16.8}Al_{22.2}Y_{0.015}Hf_{0.037}B_{0.33}C_{0.028}$

The oxidation kinetics of these alloys in the dry air is very similar, but addition of Ti did reduce the depth of internal oxidation (Unocic & Pint, 2013). In the case of the B-doped alloy, better oxide adhesion was achieved (Unocic et al., 2014). Still, the question was whether, and if so how, B and Ti are incorporated into the protective Al_2O_3-oxide layer.

In the following text, we will refer to the samples as YHf-, YHfTi-, and YHfB-sample.

Experimental Procedures

To achieve the formation of an oxide layer all samples were exposed isothermally in O_2 for 100 h at 1,100°C. High-angle annular dark field scanning transmission electron microscopy (HAADF-STEM) and energy-dispersive X-ray spectroscopy were performed using a Phillips CM 200 in Oak Ridge.

To prepare the needle shaped samples required for APT studies, a FEI VERSA 3D FIB milling station was utilized. APT needles containing two different oxide regions, the outermost part close to the surface and the inner oxide, were prepared with the FIB standard method (Larson et al., 2013). To produce APT specimens containing near-surface oxide, a magnetron sputtered Au-coating was applied. The samples were then coated with a 1 μm thick, 1 μm wide, and 15 μm long strip of Pt. After this, the sample was cut free with the ion beam and attached to an omniprobe needle. As the GBs inside the protective alumina are not visible during the preparation, the omniprobe was, rotated by 180°. Because the sample is connected to the omniprobe at an angle of 30°–50°, the procedure results in a lift-out sample produced roughly perpendicular to the surface. Subsequently, the sample was attached by Pt-deposition to a Cameca microtip flattop tip and a 1 μm thick part was cut off with the ion beam. Before the annular milling a Pt cylinder was deposited on the attached piece on top of the desired interface. By selecting this orientation, the chance of hitting a GB in the elongated samples (Fig. 1) is increased by a factor of 2. However, the final APT specimens using this procedure usually contained more Ga contamination than one prepared using the standard method. Thus, for the preparation of the outer oxide the sample pieces were attached without rotation of the omniprobe.

Analysis of the oxides with APT proved to be difficult both in terms of success rate (in our case <25%) and in terms of choice of suitable analysis parameters. Thus, the measurement parameters were studied to obtain a suitable compromise. Two different atom probes, the LEAP 3000HR at Chalmers with a green laser and the LEAP 4000HR in Karlsruhe with a UV-laser were used for the APT analyses. Generally, the LEAP 4000HR mass spectra were less complex and the peaks had smaller thermal tails (Fig. 2). In addition, the success rate of the measurements using LEAP 4000HR appeared to be higher by a factor of at least 2.

To reduce possible surface migration of mobile elements like B or C, and also to reduce differences in evaporation at phase boundaries, the measurements were performed at 25 K even though higher temperatures give alumina compositions

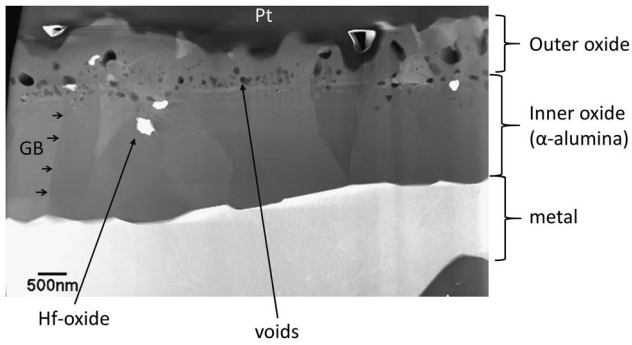

Figure 1. High-angle annular dark field scanning transmission electron microscopy of the YHfTi sample. Large grains of α-alumina form a protective inner oxide layer on top of the metal. These grains are elongated perpendicularly to the metal-oxide interface. Between them and the Pt-cover (from the preparation), the outer oxide layer, with smaller grains of alumina spinels (brighter) and the very bright HfO_2, is observed. Dark appearing voids are found between these two regions. GBs, grain boundaries.

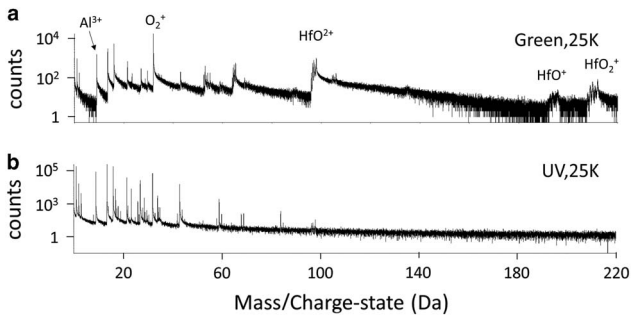

Figure 2. Mass spectra of (**a**) the LEAP 3000 with green and (**b**) the LEAP 4000 with ultraviolet (UV) laser. Typically, the thermal tails are smaller in the LEAP 4000 measurements.

closer to the stoichiometric value. The laser pulse energy was typically 200 pJ for the LEAP 3000 and 20 pJ for the LEAP 4000. The laser of the LEAP 4000 has a smaller focal point, which allows lower pulse energies. Pulse frequencies between 100 and 250 kHz were used depending on the applied voltage to avoid a mass cutoff below 300 Da. For the APT reconstructions with IVAS 3.6.12 we used SEM images, if possible. Otherwise the reconstruction was based on the reconstruction parameters (evaporation field of 25.6 V/nm, image compression factor of 1.65, k-factor of 3.3) obtained for a reference measurement of pure alumina at 25 K with 20 pJ in the LEAP 4000, in which plane distances could be identified by using cross-correlated spatial distribution maps (SDM) (Boll et al., 2012), which the paper refers to as AtomVicinity (Boll et al., 2007), an algorithm almost identical to SDM (Geiser et al., 2007).

Results

Figure 1 is a STEM-HAADF micrograph showing the oxide structure typical for all the investigated samples. It consists of α-alumina grains that form a protective layer on top of the bright imaging metal. The grains are elongated in their growth direction, i.e., perpendicular to the metal surface. They are typically about 2 μm high and 1 μm wide. On top of this region, a more finely grained region with equiaxed oxide is visible. This part of the scale originates from the oxide formed during initial oxidation and has been transformed during subsequent exposure. It consists of a mixture of alumina and spinel grains. The region also contains dark imaging voids and bright imaging small precipitates of heavy metal (Y or Hf) oxides.

Acquisition of APT data from the oxidized samples proved to be difficult. Although α-alumina itself runs quite well and measurements with several 100 millions of collected atoms were easily attainable, the successes rate of analysis of the specimens containing oxide phase or GBs was below 25% due to the early specimen fracture. Furthermore, it appeared that premature fractures of the specimens containing the outermost part of the oxide were more frequent than for the specimens containing the inner parts. This was most probably due to the presence of voids at this part of the oxide (see Fig. 1). On the other hand, it was more difficult to prepare samples containing oxide GBs in the inner part of the oxide as the oxide grain size is larger there.

Initially analyses were performed at 60 K, which gave a composition of α-alumina much closer to the stoichiometric value than the 25 K runs. However, as the lower temperature reduces the differences in evaporation fields, the local magnification effect and possible surface migration of elements like B or C, the majority of experiments was performed at 25 K.

APT Mass Spectra

The APT mass spectra collected with the LEAP 4000 are typically easier to interpret, showing smaller peak tails (Fig. 2). Concerning Hf-molecules, the spectrum is also much simpler. However, usually more hydrides were observed in the measurements, which counteracted this positive effect to some extent. The higher number of peaks leads to a situation where more tails overlap. This makes it effectively more complicated to give an exact value for the Cr and Ni concentration by deconvolution of the peaks. We decided to give these values of the oxide matrix composition as an upper limit as it is known that the solubility of alloying elements in α-alumina is extremely low (Kofstad, 1966).

Generally, nonmolecular Hf is rarely detected, instead it usually field evaporates as molecular $HfO^{+/2+/3+}$ ions and to some extent as more complex oxide molecules like HfO_2 or Hf_2O. This results in overlaps with Pt for 3 out of 4 of the significant isotopes, especially for the 2^+ state at 97, 97.5, and 98 Da. This is problematic only when plotting the Hf signal close to the protective Pt cap deposited during specimen preparation by FIB. Y has only one significant isotope, for Y^{2+} a peak is found at 44.5 Da that unfortunately is located in the thermal tail of AlO, which induces a high noise level in the corresponding atom maps. The only other significant peak found is YO^{2+} at 54.5 Da. Nonmolecular B can be easily identified, but most of the more complex ions show overlaps. A possible BO^+ main peak overlaps with Al at 27 Da, BO_2^+ would overlap likewise with AlO at 43 Da. There are also overlaps of the second highest BO^+ peak at 26 Da with Cr. As there was no peak for mono-atomic B present, we think it is unlikely that these overlaps are relevant. Ti and its oxides have a typical pattern of five isotopes, which would be easy to recognize, if present. The possible presence of an extremely small number of atoms that do not show up as a peak in the mass spectrum, was considered by looking at the distribution of the atoms at the peak positions. No indication of enrichment in GBs or phase boundaries was found for B or Ti.

The Outermost Part of the Oxide Scale (YHf-Sample)

For the reasons described above, the outer oxide's surface was successfully analyzed only in a YHf-sample (Fig. 3) below the protective Au-capping deposited on the sample surface. The local magnification effects, expected from the high evaporation field of Au, were successfully reduced using 25 K during analyses.

APT revealed many more features compared to STEM analysis such as small, <5 nm in diameter, Ni-rich grains observed at the very topmost oxide layer, i.e., below the Au-cap (Figs. 4b–4d). The grains were only found on a small fraction of the surface, accounting for about 30% of the area of the APT measurement when viewed from the top. They were surrounded by a Ni-rich spinel containing aluminum. Some enrichment of C and maybe Cr could be found in or around some of these particles (Fig. 4d). Using the isosurface of 32 at % Ni as the boundary of the particles their average composition is $Ni_{48.8}Al_{17.0}Cr_{1.4}C_{1.1}Hf_{0.3}O_{31.3}$. The compositions are also given in Table 1. The area around this region 1 in Figure 4 has a composition of $Ni_{16.6}Al_{32.3}Cr_{0.8}C_{0.3}Hf_{0.2}O_{49.8}$. Below region 1, one finds in region 2 a composition of $Ni_{17.2}Al_{30.7}Cr_{0.3}Y_{0.1}Hf_{0.1}O_{51.6}$. There are two kinds of GBs between

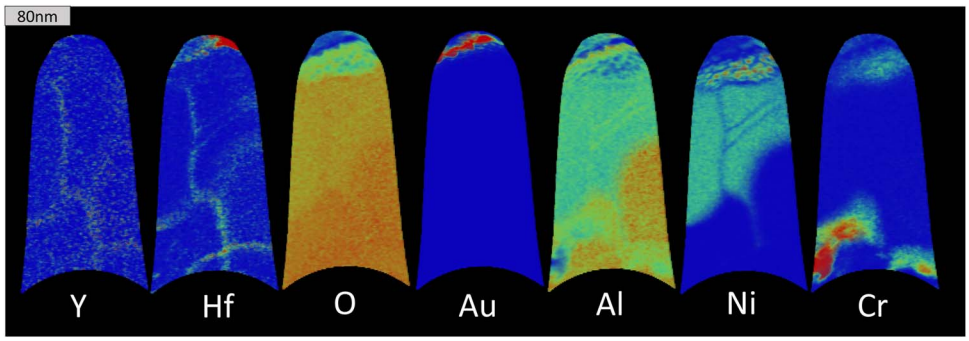

Figure 3. Atom probe tomography of a YHf-sample, prepared at the outermost part of the oxide. In the heat maps red indicates a high, and blue a low concentration. A protective Au-coating is still present on top of the oxide. The Hf at the top is incorrectly assigned Pt. Ni-spinel can be identified by observing the Ni concentration. One can see enrichment of Y and Hf at most oxide grain boundaries (GBs) and phase boundaries (PBs). In the spinel-GBs Al is enriched.

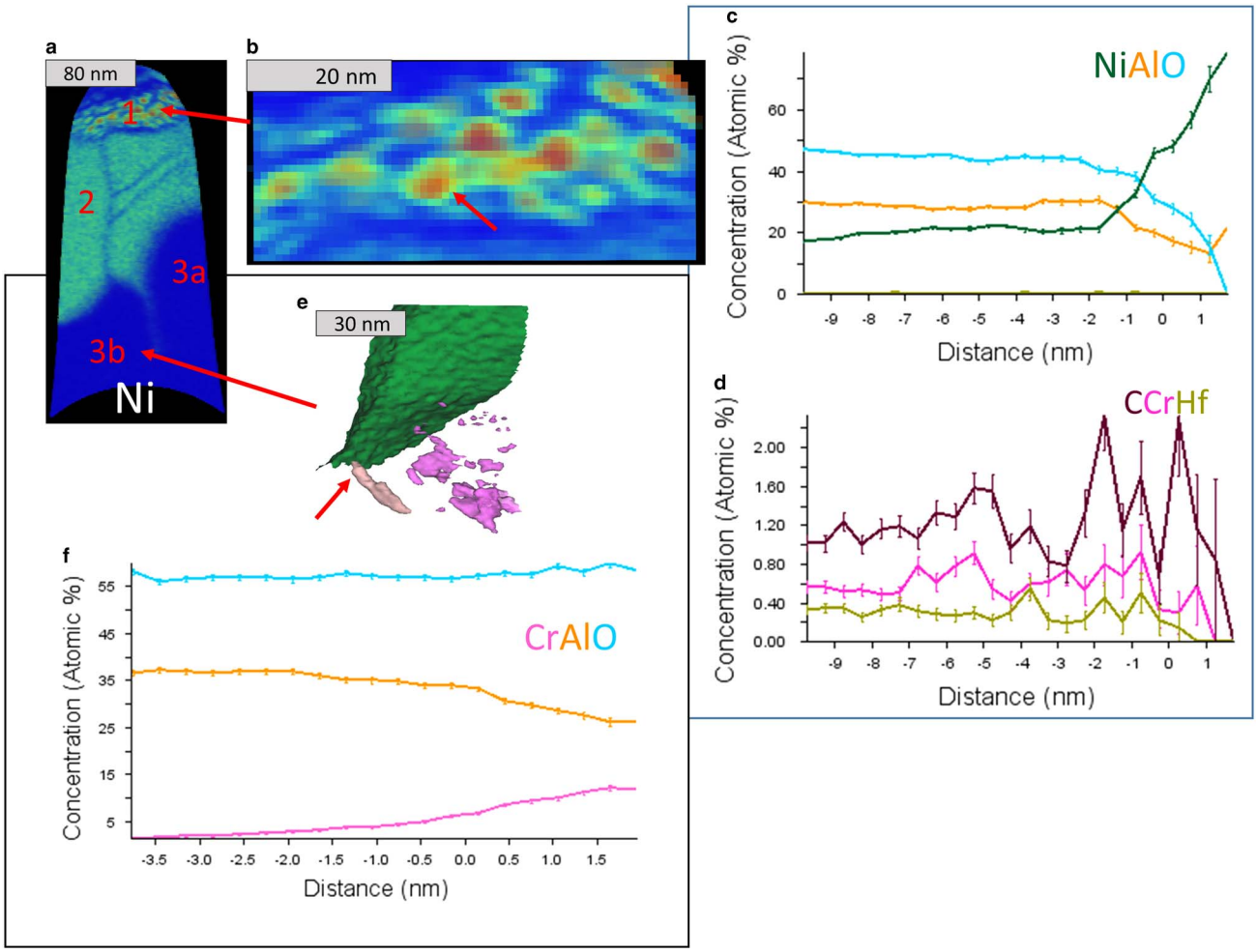

Figure 4. **a:** Several regions identified in the Ni-rich part of the YHf-sample presented in Figure 3. **b:** Magnification of the upper region containing Ni-rich particles. **c:** A proxigram of the major elements through the 32 at% Ni isosurface of the marked (red arrow) particle. Note the low O-concentration in the particle core. **d:** Same as for (**c**) but for the minor elements. Carbon is enriched in the particle in comparison with the surrounding material. Cr and Hf are depleted in the particle core. **e:** A closer look at region 3b with a green isosurface for Ni >10 at% and the pink isosurface for Cr >7 at%. **f:** The proxigram of the marked [arrow in (**e**)] Cr particle reveals that the precipitate follows the M_2O_3 composition.

different grains with this composition. One, going vertically, is heavily enriched in Hf, Y, and Al, with Gibbsian excesses of $\Gamma_{Hf} = 1.6\,nm^{-2}$, $\Gamma_{Cr} = 1.5\,nm^{-2}$, $\Gamma_{Y} = 0.1\,nm^{-2}$, $\Gamma_{Al} = 1.3\,nm^{-2}$, and $\Gamma_{O} = 2.8\,nm^{-2}$ (Table 2). Two other GBs, which are oriented at an angle of 60° to the vertical one, are parallel to each other and seem to contain less Hf , almost no Y, but do

Table 1. Measured Compositions of Oxides.

Samples	Composition
YHf (Figs. 3, 4)	
Region 1: particles	$Ni_{48.8}Al_{17.0}Cr_{1.4}C_{1.1}Hf_{0.3}O_{31.3}$
Region 1 matrix	$Ni_{16.6}Al_{32.3}Cr_{0.8}C_{0.3}Hf_{0.2}\ O_{49.8}$
Region 2	$Ni_{17.2}Al_{30.7}Cr_{0.3}Y_{0.1}Hf_{0.1}O_{51.6}$
Region 3a	$Ni_{0.1}Al_{42.6}Cr_{1.0}O_{56.3}$
Region 3b	$Ni_{0.7}Al_{34.7}Cr_{9.3}O_{55.0}$
YHfB (Fig. 5)	
Al_2O_3	$Al_{37.8}O_{62.2}$
HfO_2	$Hf_{32.4}Y_{0.2}Zr_{1.0}O_{66.4}$
YHfB Al_2O_3 (no figure)	$Ni_{<0.1}Al_{41.7}Cr_{<0.2}O_{58.0}$
YHfTi (Fig. 6) average	$Ni_{<0.1}Al_{43.6}Cr_{<0.2}O_{55.9}$

Table 2. Gibbsian Excess Values Measured at Grain Boundaries.

Samples	Gibbsian excess
YHf (Figs. 3, 4)	
Ni-spinel	$\Gamma_{Hf}=1.6\,nm^{-2}$, $\Gamma_{Cr}=1.5\,nm^{-2}$, $\Gamma_{Y}=0.1\,nm^{-2}$, $\Gamma_{Al}=1.3\,nm^{-2}$, $\Gamma_{O}=2.8\,nm^{-2}$
YHf (Fig. 5)	
Al_2O_3	$\Gamma_{Hf}=1.5\,nm^{-2}$, $\Gamma_{Cr}=1.4\,nm^{-2}$, $\Gamma_{Y}=0.64\,nm^{-2}$, $\Gamma_{Ni}=0.07\,nm^{-2}$
YHfTi (Fig. 6)	
Al_2O_3	$\Gamma_{Hf}=1\,nm^{-2}$, $\Gamma_{Cr}=6.3\,nm^{-2}$, $\Gamma_{Y}=0.1\,nm^{-2}$

contain Al. Below this spinel region, small aluminum rich grains with $Ni_{0.1}Al_{42.6}Cr_{1.0}O_{56.3}$ are present in area 3a, but also Cr-enriched areas with $Ni_{0.7}Al_{34.7}Cr_{9.3}O_{55.0}$ are present in region 3b. A closer look at this region is presented in Figure 4e, where an isosurface for Cr >7 at% is plotted. This shows that this Cr-enriched region indeed is not homogeneous, but contains several precipitates. In Figure 4f the proxigram for the marked precipitate is given. The oxygen content is the same as in the matrix, but the Al-content is lower. No enrichment of other elements was found.

The Inner Oxide (YHfB, YHfTi, and YHf Samples)

In this part of the oxide, the alumina GBs are relatively sparsely distributed so that in several APT analyses the GB was missed (despite site-specific sample preparation). These measurements could be up to several 100 nm long and the average composition of the oxide obtained using specimen temperature of 25 K was $Ni_{<0.1}Al_{43.6}Cr_{<0.2}O_{55.9}$.

In YHfB samples no GB between the alumina grains was successfully investigated and no B-signal was found in the oxide mass spectra. Instead Hf-rich oxide particles have been encountered (Fig. 5). The composition of the particles is $Hf_{32.4}Y_{0.2}Zr_{1.0}O_{66.4}$, i.e., very close to the stoichiometric value of HfO_2. The presence of Zr in the particles is not expected from the nominal composition of the alloy. Furthermore, a Y-enriched area is visible at the interface to the alumina ($Al_{37.8}O_{62.2}$). This enrichment appears rather as a Y-enriched part of the HfO_2 grain than as a mono-atomic

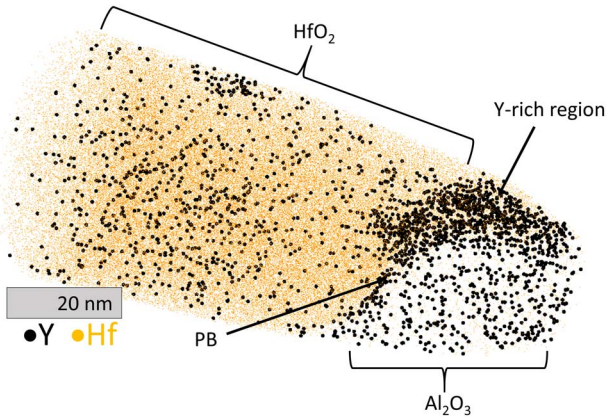

Figure 5. Atom probe tomography of a YHfB-sample in the inner oxide. The interface between a Hf_2O and a Al_2O_3 grain is presented. Y-rich region (indicating possible precipitate) attached to the phase boundary (PB) with segregated Y is visible. Yttrium signal in the oxide grains originates from noise.

layer GB segregation. No enrichment of Ni, Cr, or B at the interface was found. In addition, YHfB samples containing only oxide matrix without any interfaces were analyzed. In these measurements the composition of alumina was $Ni_{<0.1}Al_{41.7}Cr_{<0.2}O_{58.0}$ (see Table 1).

Figure 6 represents the heat map of the inner alumina region (but still close to the outer oxide) in a YHfTi sample. GBs between three different alumina grains (1, 2, and 3) are present in the analyzed volume and segregation of Hf, Ni, and Cr is apparent. However, no Ti was found at this interface. The Gibbsian excesses of the GB between grain 1 and 3 were calculated as $\Gamma_{Hf}=1\,nm^{-2}$, $\Gamma_{Cr}=6.3\,nm^{-2}$, $\Gamma_{Y}=0.1\,nm^{-2}$. Apparently the Y, which is not easily visible in Figure 6, is present, but Ni is not enriched in this part. However, the presented Gibbsian excesses have to be interpreted with caution as a Cr- and Ni-enriched region is nearby. Furthermore, the Cr content is so high that this region could be considered a precipitate. An analysis of the Gibbsian excesses of the other GBs was not possible as they are too close to each other and the analyzed GBs too small.

In Figure 7, a GB region between the α-alumina grains far away from other interfaces is analyzed for YHf. The concentration profile through the GB reveals the presence of several elements at the interface. The concentrations of other elements but Al and O in the matrix is 0 within the margin of error. To improve the visibility of the peaks, the profiles are shifted along the y axis. Again, the Gibbsian excess was calculated as $\Gamma_{Hf}=1.5\,nm^{-2}$, $\Gamma_{Cr}=1.4\,nm^{-2}$, $\Gamma_{Y}=0.64\,nm^{-2}$ and $\Gamma_{Ni}=0.07\,nm^{-2}$.

DISCUSSION

Determination of the Oxygen Content by APT

The observed deficit of O in the APT analysis of oxides is an issue discussed within the atom probe community as analyses of ceramics using APT have become possible. Until quite recently the reasons behind the missing oxygen ions

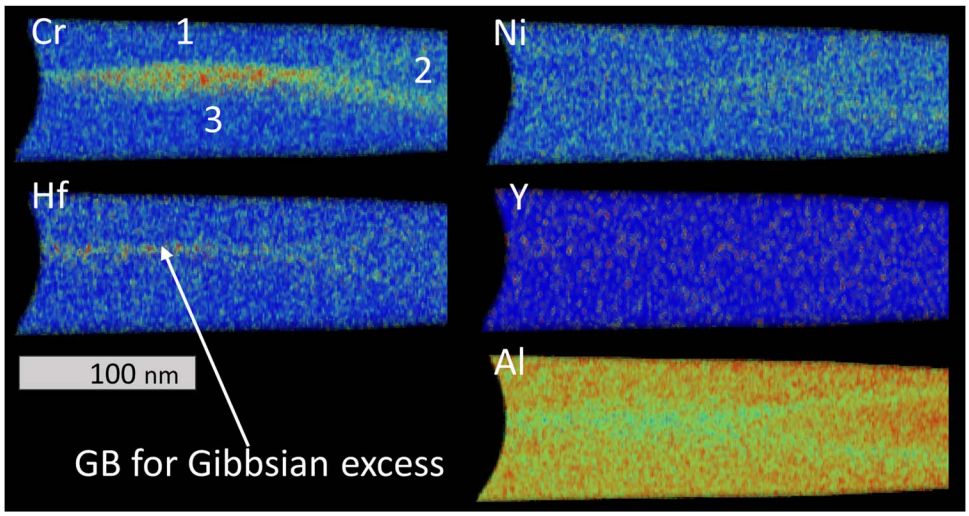

Figure 6. Atom probe tomography of a YHfTi sample below the spinel-rich region. At the alumina grain boundaries between the three grains 1, 2, and 3, an enrichment of Hf, Ni, and Cr is obvious. The enrichment of Y is barely visible due to the high noise level.

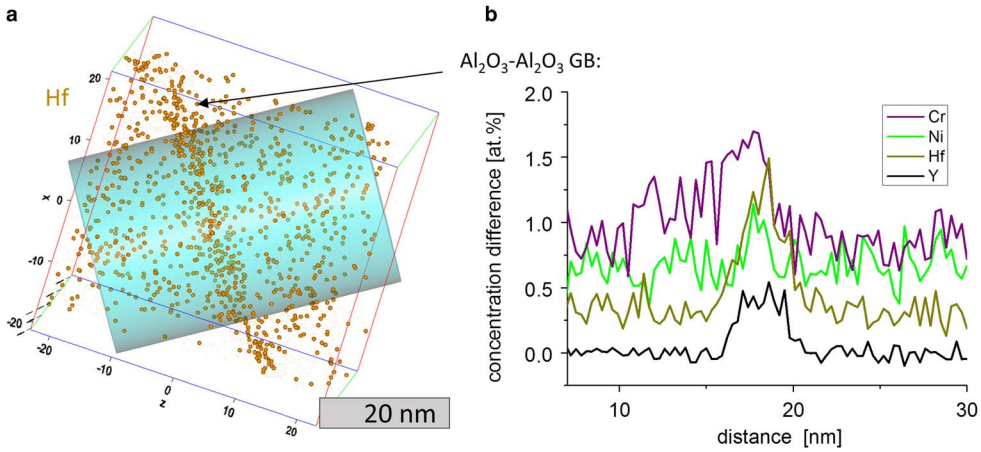

Figure 7. a: Atom probe tomography of alumina grain boundary (GB) in an YHf-sample. **b:** Concentration profiles of Y, Hf, Cr, and Ni through the GB. To visually separate the lines from each other all profiles except for Y are shifted upward. An enrichment of Y, Hf, Cr, and Ni at the GBs is visible. The concentration of all the elements outside the GB is equal to 0.

were not well understood. However, it seems that there does exist a good explanation for the observed nonstoichiometry of many oxides at present. It is proposed, with the support from density functional theory simulations for MgO, that the evaporation of oxygen as neutrals is the underlying reason for the observations (Karahka & Kreuzer, 2013). The basic idea is that field evaporated O^+ ions can recombine with oxygen at the surface and are then released as a neutral O_2-molecules, thereby being undetected. As a consequence, one may expect difficulties to differentiate between spinels, NiO, and alumina based on O content. However, it is still possible to identify the oxides based on their metallic content.

Oxide Formation

The results from APT analyses are in a good agreement with STEM investigations showing the occurrence of two different layers in the oxide scale, namely, the protective large oxide grains in the innermost part of the scale and an area with smaller equiaxed grains on the top (Fig. 1). However, APT allows for more detailed analyses with respect to the chemistry of the layers. Thus, it is possible to identify not only the Ni-rich spinel enriched in Cr (about 1 at% Cr) close to the surface, but also small precipitates with diameters of about 5 nm embedded in this spinel (see Fig. 3). Below this region another Ni-spinel, with practically no Cr and higher amount of Ni, is found. Identifying these two phases as $Al_{2-x}Ni_{1+x}O_4$ spinels is very reasonable, considering that some O is lost in the APT measurement and that Al can be replaced by Cr in the oxide. The region containing spinels is followed by an alumina layer containing areas with an average of 9 at% Cr and <1 at% Ni.

The above-mentioned findings can be explained by the oxidation process. At the very beginning, a rapid oxidation

takes place on the metal surface. This process favors not only the formation of Ni-rich spinel, but also simultaneous nucleation of various other Cr-, Ni-, and Al-oxides. After the first oxide layer is formed, the oxidation process slows down and the ability of Al and Cr to form oxides becomes higher than for Ni and thereby an Al- and Cr-rich oxide layer is formed below the Ni-rich layer. When a sufficiently thick oxide scale has been formed, the oxygen partial pressure (pO_2) at the metal/oxide interface is so low that it prevents the oxidation of elements other than Al. This results in a purer alumina oxide (α-alumina) in the innermost part of the scale, explaining why the Cr-enriched alumina is found in the outer scale region.

The Ni-rich spinel is thought to be mostly outward growing, i.e., it grows by outward diffusion of metal cations, whereas alumina is an inward growing oxide (grows by inward diffusion of oxygen through the oxide GBs), which explains the formation of the line of voids visible in the STEM images (Fig. 1) between these two oxide regions.

Existence of the nanosized precipitates embedded in Ni-rich spinel situated close to the oxide surface is somewhat puzzling. This feature was observed occasionally, and only in a limited region of the investigated sample. It is clear that the precipitates must have been produced during the later stage of oxidation as if they would have been created during the initial oxidation when Ni-spinels start to form, they would be situated close to the line of voids. One possible explanation would be that the precipitates were created as a result of healing of a micro crack in the mature scale when the bare metal was exposed to oxygen. The APT specimen could have been by chance produced so that it touches on the healed region. Further investigations are needed to reach better understanding in this matter.

Segregation to GBs and Phase Boundaries

Only inner parts of oxide scales formed on boron-rich YHfB and Ti-containing YHfTi materials were successfully analyzed by APT. No segregation of B or Ti to any of the analyzed interfaces and no precipitates rich in these elements were observed. This is consistent with previous TEM investigations (Unocic & Pint, 2013; Unocic et al., 2014), in which it is proved that the addition of B to the Ni–Cr–Al alloy does not affect the alumina scale microstructure and that there is no Ti segregation to alumina GBs in the oxide part close to the metal. Instead, TEM analyses of Ti-containing Ni-based alloys often reveal existence of Ti-rich oxide grains on the scale surface.

Contrary to boron and titanium, yttrium and hafnium both segregate to GBs between spinel grains and alumina grains and also to boundaries between different oxide phases (see Table 3). Furthermore, segregation of Ni and Cr is found at α-alumina GBs close to the surface and within the protective alumina oxide. Segregation of Y and Hf was previously reported in TEM studies (Unocic & Pint, 2013), but segregation of Ni (Fig. 7) is a new finding, indicating that there should be some growth of the outermost spinel part due to the transport of Ni even when the innermost alumina part of the scale is well developed. This statement is also supported by the observation of segregation of Cr and Al to the Ni-spinel GBs.

Table 3. Segregation of the Different Alloying Elements to the Interfaces.

	Al_2O_3–Al_2O_3	Al_2O_3–M_yO_x
Hf	Y	Y
Y	Y	Y
Ti	N	N
B		N
Ni	Y	N
Cr	Y	N

Y, Yes; N, No.

Comparison of the Gibbsian excess between GBs in the Ni-spinel and the α-alumina parts is noteworthy. It reveals that Hf and Cr populate both types of GBs to the same extent suggesting that the driving force for their segregation is the same along a net of GBs from the surface to the metal (Table 2). Y shows different values for different GBs leading to believe that its segregation may depend on local availability of this element.

Conclusions

We studied oxidation at 1,100°C of three model NiAlCr alloys with different additions of Hf, Y, Ti, and B using APT. The investigation proves the applicability of APT to oxidation issues. The efforts were directed toward analysis of the innermost part of the oxide scale being most responsible for the good resistance to the alloy degradation by oxidation. The segregation of Y and Hf to the grain- and phase-boundaries was observed confirming the importance of these elements on the oxidation kinetics of the alloys. Ti or B were found neither in the oxide matrix nor in any of the investigated interfaces. It is therefore suggested that these elements do not alter the inward diffusion of oxygen through the scale into the metal.

Noteworthy findings are the Al enrichment at GBs of Ni-spinel and Ni enrichment at alumina GBs, which can be an indication for a small amount of outward diffusion of these elements through the GBs. A complete list of all segregations can be found in Table 3. The formation of the Ni-rich precipitates close to the surface is surprising and a complete explanation of this finding has yet to be developed. Nevertheless, the general structure of the oxide scale, especially close to the interface with the air, could be explained as resulting from a shift of rapid oxidation at the beginning to diffusion of metal ions and O ions during the formation of the Ni-spinel and of another shift to predominant inward O-diffusion during the formation of the α-alumina layer.

Acknowledgments

This work is financed by Swedish Energy Agency. Julia Wagner from KNMF at Karlsruhe Institute of Technology is thanked for providing access to the LEAP 4000.

References

Boll, T., Al-Kassab, T., Yuan, Y. & Liu, Z.G. (2007). Investigation of the site occupation of atoms in pure and doped TiAl/Ti3Al intermetallic. *Ultramicroscopy* **107**, 796–801.

Boll, T., Zhu, Z., Al-Kassab, T. & Schwingenschlögl, U. (2012). Atom probe tomography simulations and density functional theory calculations of bonding energies in Cu3Au. *Microsc Microanal* **18**, 964–970.

Chen, Y., Reed, R.C. & Marquis, E.A. (2012). As-coated thermal barrier coating: structure and chemistry. *Scr Mater* **67**, 779–782.

Chen, Y., Reed, R.C. & Marquis, E.A. (2014). Interfacial solute segregation in the thermally grown oxide of thermal barrier coating structures. *Oxid Met* **82**, 457–467.

Dong, Y., Motta, A.T. & Marquis, E.A. (2013). Atom probe tomography study of alloying element distributions in Zr alloys and their oxides. *J Nucl Mater* **442**, 270–281.

Geiser, B.P., Kelly, T.F., Larson, D.J., Schneir, J. & Roberts, J.P. (2007). Spatial distribution maps for atom probe tomography. *Microsc Microanal* **13**, 437–447.

Goward, G.W. (1998). Progress in coatings for gas turbine airfoils. *Surf Coat Technol* **108–109**, 73–79.

Haynes, J.A., Pint, B.A., More, K.L., Zhang, Y. & Wright, I.G. (2002). Influence of sulfur, platinum, and hafnium on the oxidation behavior of CVD NiAl bond coatings. *Oxid Met* **58**, 513–544.

Hono, K., Ohkubo, T., Chen, Y.M., Kodzuka, M., Oh-ishi, K., Sepehri-Amin, H., Lia, F., Kinno, T., Tomiya, S. & Kanitani, Y. (2011). Broadening the applications of the atom probe technique by ultraviolet femtosecond laser. *Ultramicroscopy* **111**, 576–583.

Karahka, M. & Kreuzer, H.J. (2013). Field evaporation of oxides: A theoretical study. *Ultramicroscopy* **132**, 54–59.

Kofstad, P. (1966). *High Temperature Oxidation of Metals. 1966, 340 P*. New York, NY: John Wiley & Sons Inc.

Larson, D.J., Alvis, R.L., Lawrence, D.F., Prosa, T.J., Ulfig, R.M., Reinhard, D.A., Clifton, P.H., Gerstl, S.S.A., Bunton, J.H., Lenz, D.R., Kelly, T.F. & Stiller, K. (2008). Analysis of bulk dielectrics with atom probe tomography. *Microsc Microanal* **14**, 1254–1255.

Larson, D.J., Prosa, T.J., Ulfig, R.M., Geiser, B.P. & Kelly, T.F. (2013). Local electrode atom probe tomography. Available at http://link.springer.com/content/pdf/10.1007/978-1-4614-8721-0. pdf%5Cnhttp://link.springer.com/10.1007/978-1-4614-8721-0. Q7

Lozano-Perez, S., Yamada, T., Terachi, T., Schröder, M., English, C.A., Smith, G.D.W., Grovenor, C.R.M. & Eyre, B.L. (2009). Multi-scale characterization of stress corrosion cracking of cold-worked stainless steels and the influence of Cr content. *Acta Mater* **57**, 5361–5381.

Marquis, E.A., Yahya, N.A., Larson, D.J., Miller, M.K. & Todd, R.I. (2010). Probing the improbable: Imaging C atoms in alumina. *Mater Today* **13**, 34–36.

Naumenko, D., Pint, B.A. & Quadakkers, W.J. (2016). Current thoughts on reactive element effects in alumina-forming systems: In memory of John Stringer. *Oxid Met* **86**, 1–43.

Pint, B.A. (1996). Experimental observations in support of the dynamic-segregation theory to explain the reactive-element effect. *Oxid Met* **45**, 1–37.

Stiller, K., Thuvander, M., Povstugar, I., Choi, P.P. & Andrén, H.-O. (2016). Atom probe tomography of interfaces in ceramic films and oxide scales. *MRS Bull* **41**, 35–39.

Stiller, K., Viskari, L., Sundell, G., Liu, F., Thuvander, M., Andrén, H.-O., Larson, D.J., Prosa, T. & Reinhard, D. (2012). Atom probe tomography of oxide scales. *Oxid Met* **79**, 227–238.

Unocic, K.A., Leonard, D.N. & Pint, B.A. (2014). Effect of boron on the oxidation behavior of NiCrAlYHfTi in H_2O and CO_2 environments. *Surf Coat Technol* **260**, 17–22.

Unocic, K.A. & Pint, B.A. (2013). Oxidation behavior of co-doped NiCrAl alloys in dry and wet air. *Surf Coat Technol* **237**, 8–15.

Viskari, L., Hörnqvist, M., Moore, K.L., Cao, Y. & Stiller, K. (2013). Intergranular crack tip oxidation in a Ni-base superalloy. *Acta Mater* **61**, 3630–3639.

Young, D.J. (2016). *High Temperature Oxidation and Corrosion of Metals*, 2nd ed. ■: Elsevier. Q8